Predicting the Radio Continuum - Galaxy Emission in SHARK, the Semi-Analytical Model of Galaxy Formation

Samuel Hansen

under the supervision of

Dr. Claudia Lagos

This thesis is presented in partial fulfilment of the requirements for the Master of Physics (Astrophyscs)

School of Physics, Mathematics and Computing

The University of Western Australia
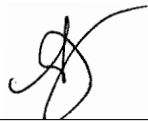
Declaration

This is to certify that:

1. This thesis comprises of my original work.

2. Due acknowledgement has been made in the text to all other materials used.

3. This thesis consists of no more than 40 pages inclusive of tables and figures but exclusive of references and appendices.

I authorise the Head of the Department of Physics to make a copy of this thesis to any person judged to have an acceptable reason for access to the information, i.e., for research, study or instruction.

Andrew Sullivan
Student ID: 22466998

Signature: Date: 17 October 2022.

Chris Power

Signature: ChrisPower.   Date: 17 October 2022.

Acknowledgements

I would like to acknowledge that this work has been completed at the University of Western Australia, which is situated on Noongar land, and that the Noongar people remain the spiritual and cultural custodians of this land.

Abstract

TEXT

Contents

Chapter 1

Introduction

1.1 Introduction

1.1.1 The Far-Infrared Radio Correlation

Planck Collaboration et al. (2016) The Far-Infrared Radio Correlation (FIRC) is an observed tight correlation between a population of galaxy's total Far-Infrared (FIR) luminosity and total radio luminosity that spans five orders of magnitude (Van der Kruit (1971), Van Der Kruit (1973), De Jong et al. (1985), Helou et al. (1985), Condon (1992)). It has been shown to exists in a variety of different galactic populations including Sub-Millimetre Galaxies (SMGs) (Thomson et al. (2014), Algera et al. (2020)), (Ultra)-Luminous Infrared Galaxies (ULIRGs) (Lo Faro et al. (2015)), Early Type galaxies (Omar & Paswan (2018)), dwarf galaxies (Shao et al. (2018)), low-ionization nuclear emission-line region (LINERs) and Seyferts (Solarz et al. (2019)), irregular and disk-dominated galaxies (Pavlović (2021)) as well as highly lensed galaxies (Giulietti et al. (2022)), to name a few.

It is often parameterised as it first was in Helou et al. (1985) as in equation 1.1

$$q_{ir} = \log_{10}\left(\frac{L_{IR}}{3.75 \times 10^{12} \mathrm{Wm}^{-2}}\right) - \log_{10}\left(\frac{L_{1.4\mathrm{GHz}}}{\mathrm{Wm}^{-2}\mathrm{Hz}^{-1}}\right), \tag{1.1}$$

where L_{IR} is total FIR integrated over $8 - 1000\mu$m in the rest frame and $L_{1.4\mathrm{GHz}}$ the total rest frame radio luminosity at 1.4GHz. While this is the most common parameterisation (Helou et al. (1985), Condon (1992), Bell (2003) etc.) the FIRC has been shown to exist using different frequency combinations as well (ie radio luminosity at 150MHz (Read et al. (2018)), infrared being a combination of 60μm and 80μm (Yun et al. (2001)) and a variety of different individual infrared frequencies (Smith et al. (2014))).

The FIRC's persistence across different magnitudes of luminosity and varied galactic populations makes it an attractive tool. It's uses include identifying Active Galactic Nuclei (AGNs) (Donley et al. (2005), Norris et al. (2006), Algera et al. (2020)), in defining the SFR-Radio correlation (Bell (2003),Condon & Ransom (2016),Duncan et al. (2020),Molnár et al. (2021)), in determining the distance to SMGs (Yun & Carilli (1999)) and deriving a galaxy's radio emission based on

1. INTRODUCTION

its IR emission (Dale et al. (2014)).

It is therefore important that we totally understand the FIRC and its limitations. In particular understanding any possible evolution the FIRC has with redshift (z). This is a very active area of research into FIRC and has some studies finding that there is some evolution with z (Ivison et al. (2010a), Ivison et al. (2010b), Magnelli et al. (2015), Delhaize et al. (2017)) and others finding no evolution (Appleton et al. (2004), Jarvis et al. (2010),Sargent et al. (2010), Bourne et al. (2011), Mao et al. (2011), Duncan et al. (2020), Thomson et al. (2014), Algera et al. (2020)). Delvecchio et al. (2021) did not find that qir evolved significantly with z, but instead evolved with stellar mass. Reasons that have been suggested for these differences include choice of spectral index (Delhaize et al. (2017)), use of IR or radio biased samples (Sargent et al. (2010)) and use of statistically insignificant samples (Jarvis et al. (2010)). However the most commonly cited reason is AGN contamination. Even high precision instruments are biased towards high mass and low redshift objects and determining the presence of an AGN in high redshift galaxies is particularly difficult (Delvecchio et al. (2021)).

Despite the wealth of research that has been conducted into the FIRC, our theoretical understanding is quite limited. Fundamentally the FIRC is grounded in star-formation where galaxy's IR and Radio emission come from the same young, massive stars. These stars, formed in dusty, molecular clouds, would emit UV radiation which is subsequently absorbed and re-emitted by these clouds at IR wavelengths. These same stars would ionise HII regions causing free-free emission and when these stars finally die, undergo a core-collapse supernova (CCSN) accelerating cosmic rays as synchrotron radiation (Condon & Ransom (2016)).

However, this simple star-formation model does not account for the FIRC in starbursts. The power of each cosmic ray electron is proportional to the magnetic energy density and hence proportional to the magnetic field of a galaxy. So a powerful starbursting galaxy (with B 1000μG) with emit much more powerful cosmic rays that a normal spiral (with B 100μG) (Condon & Ransom (2016)). The calorimeter model proposed by Völk (1989) to explain this discrepancy. The assumption is that the lifetime of a cosmic ray electron is proportional to the inverse of the magnetic energy density. Thus, cosmic rays from starbursting galaxies can still be powerful, but only radiate a short time, whereas cosmic rays from normal galaxies at a lower power, but for a propotionally longer time. It's from this understanding of radio emission that Bressan et al. (2002) developed their model for modelling radio emission.

The calorimeter model leads to three assumptions; that galaxies are electron calorimeters, UV calorimeters and that synchrotron radiation is the main loss mechanism. These assumptions are unlikely to be true (Lacki et al. (2010)). Consequently, to explain the FIRC, a number of conspiracies have been suggested. For example Lacki et al. (2010) found that in normal galaxies, when electron calorimetry decreases the radio emission, decreasing UV opacity increases the IR emission. For starbursts, Lacki et al. (2010) found that bremsstrahlung, ionization, and IC losses decrease the synchrotron emission, but this is balanced by secondary electrons and the fact that 1.4GHz observation probe lower cosmic ray energies when magnetic field strength increases. In another conspiracy, Bell (2003) found that IR and Radio are not proportional to

the SFR of a galaxy, but they are disproportional to SFR in complimentary ways that cancel each other out.

With the invocation of uncomfortably well-tuned parameters and potential for new physics it is not surprising that the FIRC has enticed a wealth of studies. This has included some models that have ranged from one-zone model of cosmic ray injection (Lacki et al. (2010)), a 1D model of turbulent clumpy star-forming galactic disks (Vollmer et al. (2022)) and a semi-analytic model (SAM) of a single, idealised galaxy (Schober et al. (2022)). In this paper we use SHARK, a semi-analytic model of galaxy formation to model the FIRC without invoking any conspiracy. As far as we can assess, there is no other model of galaxy formation that also models the FIRC. This makes SHARK the first to directly model a large population of galaxies over cosmic time to include L_{IR}, L_{rad} and consequently qir.

Chapter 2

Methods

2.1 Methods

In this model. we model radio emission as two parts: Free-Free emission and synchrotron emission.

2.1.1 SHARK

SHARK is an open source, semi-analytic model of galaxy formation first presented in Lagos et al. (2018). In this paper we use SHARK v1.1 which is the same presented in Lagos et al. (2018). This version uses the Synthetic UniveRses For Surveys (SURFS) simulation suite (Elahi et al. 2018), specifically the L210N1536 simulation, which uses a ΛCDM (Planck Collaboration et al. 2016) cosmology. That is a Hubble constant of H_0 = h $\times$ 100(km/s)/Mpc, h = 0.6751, matter density of Ω_m = 0.3121, baryon density Ω_b = 0.0491 and dark energy density of Ω_Λ = 0.6879. The SURFS L210N1536 simulation has a boxsize of L_{box} = 210cMpc/h and a softening length ϵ = 4.5ckpc/h. Each box contains N_{p} = 1536^3 dark matter particles each with a mass of m_{p} = 2.21 $\times 10^8 M_\odot$/h. The SURFS simulation suite allows for studies of galaxies with stellar masses above $10^7 M_\odot$. This simulation produces 200 snapshots logarithmically arranged from z = 24 $-$ 0. This corresponds to a time between snapshots of $\approx$ 6 $-$ 80Myr.

Halos, subhalos and their properties are identified using VELOCIraptor (Elahi et al. 2019a, Cañas et al. 2019). VELOCIraptor first identifies halos using a 3D friend-of-friend (FOF) algorithm. It also applies a 6D FOF with velocity dispersion to remove spuriously linked objects (like early stage mergers). This 3D FOF structure corresponds to the halo. It then identifies particles that have a local velocity distribution significantly different from the smooth background halo. It runs a phase-space FOF on these particles to identify the subhalos. SURFS only considers halos with $/rm \geq$ 20 dark matter particles.

Merger tress are then constructed using TreeFrog (Elahi et al. 2019b). At it's most basic, TreeFrog is a particle correlator that relies on particle IDs being continous across snapshots. The merger tree is constructed forward in time, indentifying the optimum link between progenitors and descendants. TreeFrog searches up to four snapshots to identify optimal links.

VELOCIraptor and TreeFrog provide the subhalo and merger tree catalogues, respectively, which provide the basis from which galaxies are evolved. Shark evolves these galaxies across snapshots using a physical model. The physical model used here is fully described by equations 49-64 in Lagos et al. (2018). Before this evolution takes place, the merger trees undergo a post processing treatment.

First 'interpolated' subhalos are inserted between snapshots of the current subhalo and its descendants. This interpolated subhalo has the same properties as the progenitor subhalo. This ensures continuity of galaxy evolution across snapshots. Since TreeFrog searches up to four snapshots for primary links, it is possible that a descendant subhalo is not present in the following snapshot, thus causing discontinuity. The interpolated subhalos solve this problem and enforces continuity of galaxy formation.

Second, the merger tree is checked to make sure that the mass of each halo is strictly equal to larger than the halo mass of its most massive progenitor. This ensures a matter accretion rate onto halos is always ≥ 0.

Third, the central subhalos are found. At the z = 0 snapshot, the most massive subhalo of every existing halo is defined as the central subhalo. The main progenitor of this central subhalo is then defined as the central subhalo of their repspective halos in the next snapshot and so on back through time. Other subhalos that are not the main progenitor or the most massive subhalo of an existing halo are designated satellite subhalos.

Finally, halos that first appear in the catalogue (the ones without a progenitor) are identified. The central subhalo of this halo is assigned a halo gas reservoir of mass $\Omega_{\mathrm{b}}/\Omega_{\mathrm{m}} \times M_{\mathrm{halo}}$ (where M_{halo} is the mass of the halo). Gas cooling is ignited when halo gas mass is > 0, and so a cold gas disk is formed. After each snapshot, the galaxies that are hosted by a subhalo are transfered to their descendants and evolved. If a halo is formed without a progenitor and is a satellite subhalo it is defined as a dark subhalo, is not assigned any gas and does not evolve.

Within Shark there are three different types of galaxies; Centrals, which are the central galaxy of the central subhalo, Sattellites, which are the central galaxy of satellite subhalos and Orphans, which are the central galaxy of a defunct subhalo. A defunct subhalo is one which has merged onto another subhalo and is not the main progenitor. From these definitions a central subhalo can have only one central galaxy, but many orphan galaxies, but a satellite subhalo can only have one satellite galaxies.

In this paper we scale up the total volume of each snapshot by utilising 64 independent sub-volumes. Each sub-volume is a box with $V_{\mathrm{box}} = 210^3 [\mathrm{cMpc/h}]^3$ independently evolved from other sub-volumes. This means the total volume under consideration is $V_{\mathrm{total}} = 64 \times 210^3 [\mathrm{cMpc/h}]^3$ in this paper. By increasing the volume, and therefore number of galaxies, being considered we can construct a more robust population of galaxies from which to derive properties. Shark uses the universal Chabrier IMF (Chabrier 2003).

2. METHODS

2.1.2   Viperfish and ProSpect

This work builds on the galaxy emission models presented in Lagos et al. (2019). This includes using the Spectral Energy Distribution (SED) created for FIR-FUV emission of SHARK galaxies. These SEDs are created using PROSPECT (Robotham et al. 2020) and VIPERFISH (Lagos et al. 2019).

PROSPECT is a generative SED package that allows for the creation of SEDs from known star formation and metallicity histories. It can also be used to fit observed SEDs VIPERFISH is an intermediary tool that connects SHARK with PROSPECT. VIPERFISH extracts star formation histories (SFH) and metallicity formation histories (ZFH) from SHARK and translates them to PROSPECT for SED generation.

PROSPECT was designed to be user friendly with high levels of flexibility in the SFH and ZFH inputs. PROSPECT can make use of the Bruzual & Charlot (2003) or Vazdekis et al. (2016) stellar synthesis libraries and uses a Chabrier (2003) IMF for both libraries. This gives PROSPECT a broad spectral range available for SED generation from stellar synthesis library that is well understood by the astrophysics community. In this paper we use the Bruzual & Charlot (2003) stellar synthesis library and the Chabrier (2003) IMF. This is the same stellar synthesis library used to produce SEDs in Lagos et al. (2019) and the same IMF used in SHARK (Lagos et al. 2018).

PROSPECT's flexibility in its SFH and ZFH inputs makes it ideal for use with SHARK. In PROSPECT, SFH and ZFH can be arbitarily complex; internal interpolation schemes map the provided inputs onto the discrete library of temporal evolution available. Note that if the timesteps within the provided ZFH and SFH are too large this can lead to large uncertainties in the resulting emission, particularly UV. In SHARK, the UV emission is accurately predicted as the time-steps are sufficiently fine (Lagos et al. 2019).

PROSPECT generates SEDs from SHARK by using a simplified fiducial model of dust processing. The light is first attenuated by the Charlot & Fall (2000) dust model. The dust is assumed to be in two phases; birth clouds (BC) and diffuse ISM. The absorption curves for the BCs and ISM are defined in Equations 2.1 and 2.2.

$$\tau_{\mathrm{ISM}} = \hat{\tau}_{\mathrm{ISM}}(\lambda/5500\text{Å})^{\eta_{\mathrm{ISM}}}, \tag{2.1}$$

$$\tau_{\mathrm{BC}} = \tau_{\mathrm{ISM}} + \hat{\tau}_{\mathrm{BC}}(\lambda/5500\text{Å})^{\eta_{\mathrm{BC}}}, \tag{2.2}$$

where τ_{BC} and τ_{BC} are the optical depths at 5500Å for BC and the diffuse ISM respectively, τ_{BC} and τ_{ISM} are the attenuation due to BC and ISM respectively. η_{ISM} and η_{BC} are the spectral slopes for the two attenuation curves.

Light from different stellar age populations are attenuated by dust differently. Birth clouds contain stellar populations younger than 10 Myr and older stars are not present in birth clouds. Hence, light from younger stars has its light attenuated by both Eqns 2.1 and 2.2 while older

stars are only attenuated by Eqn 2.2.

For the calculation of τ_{ISM}, τ_{BC} and η_{ISM} it is necessary to calculate the surface density of dust (Σ_{dust}). In SHARK the calculation of Σ_{dust} is done separately for disks and bulges. For disks the average Σ_{dust} is given by:

$$\Sigma_{\text{dust,disk}} = \frac{M_{\text{dust,disk}}}{2\pi r_{50,d} l_{50}} \tag{2.3}$$

where $M_{\text{dust,disk}}$ is the dust mass in the disk, $r_{50,d}$ is the half-gas mass radius of the disk (both of these quantities are outputs in the HDF5 file from SHARK) and l_{50} is the projected minor axis. Here $l_{50} = \sin(i) * (r_{50,d} - r_{50,d}/7.3$ where i is the inclination. 7.3 is the scaleheight to sclelength observed relation in local galaxy disks (Kregel et al. 2002). A galaxy's inclination is determined by the host subhalo angular momentum vector or is randomly chosen for orphan galaxies (Chauhan et al. 2019).

For bulges the average Σ_{dust} is given by:

$$\Sigma_{\text{dust,bulge}} = \frac{M_{\text{dust,bulge}}}{2\pi r_{50,d}^2} \tag{2.4}$$

where $M_{dust,bulge}$ is the dust mass in the bulge and $r_{50,b}$ is the half mass radius of the bulge. Inclination is not important in bulges because we assume they are spherically symmetric.

For attenuation due to the diffuse ISM, Lagos et al. (2019) use the work of Trayford et al. (2017) and Trayford et al. (2019).

Trayford et al. (2017) computed the attenuation for each galaxy in the EAGLE hydrodynamical simulation suite using SKIRT (a software package that can be used for simulating radiation transfer in galaxies). These curves were later parameterised to the Charlot & Fall (2000) model (Trayford et al. 2019). From these parameterised curves the median and $1 - \sigma$ relationship between τ_{ISM}, η_{ISM} and Σ_{dust} were derived. Using these parametrerised curves and the Σ_{dust} from SHARK as calculated in Eqns 2.3 and 2.4 τ_{ISM} and η_{ISM} are calculated. These values are then perturbed by sampling from a gaussian disrtibution with width σ, where σ is the $16^{\text{th}} - 84^{\text{th}}$ percentile as predicted by Trayford et al. (2019).

Lagos et al. (2019) follows the Lacey et al. (2016) model for birth cloud attenuation. This model assumes that the birthcloud optical depth scales with the gas metallicity and gas surface density of the cloud, but substitutes the metal surface density with dust surface density of the clouds:

$$\tau_{\text{BC}} = \tau_{\text{BC,0}} \left(\frac{f_{\text{dust}} Z_{\text{gas}} \Sigma_{\text{gas,cl}}}{f_{\text{dust,MW}} Z_{\odot} \Sigma_{\text{MW,cl}}} \right) \tag{2.5}$$

where $f_{\text{dust}} = M_{\text{dust}}/M_{\text{Z}}$, (dust-to-metal mass ratio), $\tau_{\text{BC,0}} = 1$, $\Sigma_{\text{MW,cl}} = 85 M_{\odot}\text{pc}^{-2}$, $Z_{\odot} = 0.0189$ and $f_{dust,MW} = 0.33$ so that a typical sprial galaxy, $\tau_{\text{BC}} \approx \tau_{\text{BC,0}}$ (matching the result from Charlot & Fall (2000) and Kreckel et al. (2013)).

The cloud surface density is $\Sigma_{\text{gas,cl}} = \max[\Sigma_{\text{MW,cl}}, \Sigma_{\text{gas}}]$ where Σ_{gas} is found using Eqs. 2.3 and 2.4. Galaxies in the local group have a giant molecular cloud with constant gas surface

2. METHODS

density close to the value of $\Sigma_{MW,cl}$ (Krumholz 2014). This gas surface density is independent of galactic environment and has been found in galaxies ranging from metal-poor dwarfs to molecule-rich spirals. Outside of the local group, the giant molecular cloud surface density increases to maintain equilibrium pressure with increasing ISM pressure. Thus, $\Sigma_{\mathrm{gas,cl}} \approx \Sigma_{\mathrm{gas}}$ in these environments (Krumholz et al. 2009). A physical limit of $\mathrm{tau}_{\mathrm{BC}} \geq \tau_{\mathrm{ISM}}$. For birth blouds, Lagos et al. (2019) adopts $\eta_{\mathrm{BC}} = -0.7$, being the default value from Charlot & Fall (2000).

Once the light has been attenuated by the dust model, it must be re-emitted at longer wavelengths. To do this, PROSPECT adopts the empirical templates from Dale et al. (2014) (henceforth the Dale model).

The Dale model has been in development since 2001 and consists of observationally constrained templates to model the complete SED of normal star-forming galaxies (SFG). It is an empirical model largely based on the observations of the local Universe and was initially developed for SFGs and only for the infrared SED (between $3 - 1,100\mu m$ Dale et al. (2001). Based largely on the work of Désert et al. (1990), the Dale model combines the contributions to the SED from large dust grains, very small dust grains and polycyclic aromatic hydrocarbons (PAH) heated by radiation fields of intensity U, with U having a range of $0.3 - 10^5$. Here U measure multiples of the local interstellar radiation field in the Solar Neighborhood; $U = 1$ corresponds to the local interstellar radiation field in the Solar Neighborhood.

The Dale model adopts the same large dust grain emission profile as Désert et al. (1990) using greybody emission, the amplitude and wavelength of which varies with U. For very small dust grains the Dale model combines the result of Draine & Anderson (1985) and Tran et al. (2001). Draine & Anderson (1985) found the temperature distribution for a variety of graphite grain sizes. They showed that graphite grains of size $0.02\mu m$ will radiate at a single temperature around 20K, smaller graphite grains will radiate over much larger temperature ranges. However, this was only done for a small range of heating intensities. Tran et al. (2001) showed that small dust grain temperature distribution profiles are equivalent to temperature distribution profiles of larger grains. The Dale model combines these two results and employs the approach from Désert et al. (1990) of integration of flux normalisation of the very small grain emission curves to construct very small dust grain profiles for $U = 0.3 - 10^5$.

For PAH's, the Dale model adopts the PAH spectrum model from Désert et al. (1990), but inserts splices of observed mid-IR spectrum from their own observations made using the Infrared Astronomical Satellite (IRAS) and ISOCAM broadband observations. These are further scaled by integrating over the 12 μm IRAS filter, to construct the emission curve for PAH's.

The large dust grain, very small dust grain and PAH emission profiles are then superimposed upon each other using relative contribution ratio of 64:4.7:4.3 (large dust grains: very small dust grains: PAHs) as per Désert et al. (1990). This results in what is referred to as a 'local' SEDs: synthetic SEDs for a range of dusty environments.

In order to construct a 'global' SED or that of a galaxy the Dale model assumes a power-law

distribution in a given galaxy of dust mass over heating intensity:

$$dM_d(U) \propto U^{-\alpha}dU, 0.3 \le U \le 10^5,$$
(2.6)

where $dM_d(U)$ is the dust mass heated by a radiation field intensity U and α represents the relative contributions of different local SEDs. By convolving this semi-empirical model with Infrared Space Observatory (ISO) and IRAS broadband filter bandpasses, Dale et al. (2001) was able to reproduce the SED of galaxies observed using ISO and IRAS in the infrared.

For the generation of SEDs using PROSPECT, we adopt an $\alpha = 3$ for the diffuse ISM and $\alpha = 1$ for birthclouds. These values approximately correspond to effective dust temperatures of $20 - 25$K for the ISM and $50 - 60$K for birth clouds. We also assumed no AGN emission is present (which is left for future work).

By adding the attenuated stellar light with the dust emission together we can create the full generative spectrum. This observed frame is then redshifted using the full spectral resolution available. The spectrum is then passed through a number of filters to span the FUV to FIR for the final outputs. These results do not include nebular emission lines and is only based on broad band emission.

In the 2014 update to the Dale model (Dale et al. 2014), the radio part of the SED was added meaning that the Dale model spans from infrared to the radio spectrum. This means that it is possible to create an SED of a star forming galaxy (SFG) from the infrared to the radio using VIPERFISH and PROSPECT as described above. This extention was implemented using the infrared-radio correlation (qir). By assuming a constant qir, it is trivial to find the corresponding radio luminosity from a given infrared luminosity. However, assuming a constant qir is problematic. Recent observational results have brought in to question the rigidity of this constant qir and later in this paper we show that a constant qir cannot be assumed for all SFGs. Consequently we utilise a different method of finding the radio spectrum that is independent of the infrared light produced by the Dale model. This method, which we discuss in the next sections, was developed in Bressan et al. (2002) and Obi et al. (2017) and henceforth will be referred to as the B02 and O17 respectively.

2.1.3 Free-Free Radiation

When a particle is accelerated by an electric field, free-free radiation is produced (Condon (1992)). Free-free radiation (also known as thermal emission) occurs where an electron has its path deflected by the presence of another charged particle (it is so called free-free emission since the electron is free before and after the interaction with the particle) (Condon & Ransom (2016)).

We model free-free radiation to be proportional to the production rate of Lyman continuum photons. Lyman continuum photons are those with a wavelength smaller than 921Åwhich are responsible for completely ionising hydrogen. Young, massive stars produce large amounts of

2. METHODS

Lyman continuum photons which, when incident to the hydrogen gas region surrounding a star completely ionises the hydrogen present. This then leads to an abundance of electrons and positive ions in these regions (known as HII regions or Strömgen Spheres (Strömgren (2013))) hence many electron-ion interactions can take place leading to free-free radiation (Condon & Ransom (2016)). This is the approach used in Bressan et al. (2002) and Obi et al. (2017) which is based on the work of Rubin (1968) and Condon (1992).

The production rate of Lyman continuum photons Q_H is commonly expressed in Eq. 2.7.

$$Q_H = \int_0^{\lambda_0} \left(\frac{\lambda L_\lambda}{hc} \right) d\lambda, \tag{2.7}$$

where λ_0 is the Lyman limit, 921 Å, L_λ is the composite SED of a galaxy in ergs^{-1} Å^{-1}, h is Planck's constant and c is the speed of light. L_λ is sourced from SEDs created using the PROSPECT and VIPERFISH models as discussed in section 2.1.

Rubin (1968) (henceforth Rubin) was the first to quantify the relation between free-free radiation and the number of Lyman continuum photons. While the proof of which will not be reproduced here, Rubin starts by considering that the production rate of Lyman continuum photons will equal the destruction rate of Lyman continuum photons. Lyman continuum photons are destroyed during the photo-ionisation processes of ionising hydrogen. Rubin combines this creation-destruction equilibrium with the expression for free-free radiation total flux density from Oster (1961) and Mezger & Henderson (1967). A key assumption of the free-free radiation total flux density from Oster (1961) and Mezger & Henderson (1967) is that the frequency is large enough to ignore self-absorption.

This leads to the relation that approximates total flux density of free-free emission as a function of the number of Lyman continuum photons, temperature, frequency and distance. There is also a self-absorption term present in this equation, however as Rubin notes, for most galaxies it is possible to ignore self-absorption.

Condon (1992) would later re-express this approximation to be between luminosity, production rate of Lyman continuum photons, temperature and frequency, which is given in Eq. 2.8, In this paper, we model Free-Free radiation in the same way as in B02 and O17 in Eq. 2.8. This model is well understood theoretically and was developed by in Rubin (1968) and Condon (1992).

$$\frac{L_{ff}}{WHz^{-1}} = \frac{Q_H}{6.3 \times 10^{32} s^{-1}} \left(\frac{T}{10^4 K} \right)^{0.45} \left(\frac{\nu}{GHz} \right)^{-0.1} \tag{2.8}$$

Equation 2.8 is used in this model to calculate the free-free radiation and is identical to that used in O17 (See Equation 5 in that paper). Note that this equation is of the same form of the equation used to model free-free radiation in B02, but uses a different constant in the denominator of the production rate of Lyman continuum photons; B02 and we use $6.3 \times 10^{32} s^{-1}$ and B02 ses $5.495 \times 10^{32} s^{-1}$. (See Equation 1 in B02). B02 used their own simulation model of HII regions to calculate an average relation at 1.49 GHz to find $5.495 \times 10^{32} s^{-1}$. In this paper,

we elect to use $6.3 \times 10^{32} \text{s}^{-1}$ since it comes from a purely theoretical understanding of free-free radiation.

We assume a constant temperature of 10^4K which aligns with observations of HII regions (Anderson et al. 2009).

2.1.4 Synchrotron Emission

When a particle is accelerated by a magnetic field magnetobremsstrahlung (magnetic braking radiation) is produced (Condon & Ransom (2016)). The characteristic of the radiation produced can change depending on the speed of the electron being accelerated. Electrons travelling at ultra-relativistic speeds produce synchrotron radiation (also known as non-thermal radiation), which can account to up to 90 percent of light from SFGs at radio wavelengths (Condon (1992)). The physics behind synchrotron radiation is not as well understood as free-free radiation. As with free-free emission, we take the approach taken by B02 and O17. Relativistic electrons accelerated by core-collapse supernovae (CCSN) into the ISM is used as the dominant mechanism of synchrotron radiation with a minor contribution from supernova remnants (SNR) also included. Synchrotron radiation is calculated through Eq. 2.9, which identical to equation 17 in B02.

$$\frac{L_{sync}(\nu)}{[10^{23}WHz^{-1}]} = \left[E^{SNR}\left(\frac{\nu}{1.49GHz}\right)^{-0.5} + E^{EI}\left(\frac{\nu}{1.49GHz}\right)^{-\alpha} \right] \times \frac{\nu_{CCSN}}{[yr]}, \quad (2.9)$$

where E^{SNR} is the energy contribution from SNR, E^{EI} is the energy of electrons injected per SN event, α, the radio slope from electrons injected per SN event and ν_{CCSNe} is the rate of CCSN. In this equation we assume that E^{SNR}, E^{EI} and α are constants and take the values $\text{E}^{\text{SNR}} = 1.16 \times 10^{22}\text{WHz}^{-1}$, $\text{E}^{\text{EI}} = 1.82 \times 10^{23}\text{WHz}^{-1}$ and $\alpha = 0.816$. The values these constants take are derived empirically and differ from those used in the B02 and O17; we change the rate of CCSN within the Galaxy to match the IMF of SHARK when deriving these constants. The derivation and assumptions made within remain the same as that in B02. Later in this section, we present the brief derivation of these constants for completeness.

In Equation 2.9 ν_{CCSN} is not assumed to be constant, but instead calculated from the adopted IMF:

$$\frac{\nu_{\text{CCSNe}}}{[\text{yr}^{-1}]} = \frac{\alpha_{\text{CCSNe}}}{[\text{M}_\odot^{-1}]} \times \frac{\text{SFR}}{[\text{M}_\odot/\text{yr}]}. \quad (2.10)$$

In this paper, we adapt the model to directly calculate ν_{CCSNe} for each galaxy in SHARK. ν_{CCSNe} is modelled as directly dependent on the Star-formation rate (SFR) of a galaxy through Equation 2.10 where α_{CCSNe} is the fraction of stars that undergo CCSNe per unit solar mass formed.

It is a common assumption that the stars that eventually undergo CCSNe exist within the

2. METHODS

mass range of 8 $M_\odot \lesssim M \lesssim 50\ M_\odot$ (Heger et al. (2003), Ando et al. (2003), Nomoto (1984), Tsujimoto et al. (1997)). Above this maximum mass, stars undergo hypernova and causing Gamma Ray Bursts (Van den Heuvel & Yoon 2007). Consequently α_{CCSNe} can be expressed as it is in Equation 2.11 where $\psi(M)$ IMF.

$$\alpha_{CCSNe} = \frac{\int_{8M_\odot}^{50M_\odot} \psi(M)dM}{\int_{0.1M_\odot}^{100M_\odot} M\psi(M)dM} \tag{2.11}$$

As discussed in Section 2.1, we use the use the stellar synthesis library from Bruzual & Charlot (2003) when craeting the SEDs using PROSPECT. The Bruzual & Charlot (2003) stellar synthesis library has a mass range of $0.1M_\odot$ to $100\ M_\odot$ (hence the mass range chosen in the denominator of Equation 2.11). Both PROSPECT and the Bruzual & Charlot (2003) stellar synthesis library make use of the Chabrier (2003) IMF, ,where A = 0.158 $(\log M_\odot)^{-1}$ pc^{-3}, $m_c = 0.079$, $\sigma = 0.69$ and B = 4.43×10^{-2} $(\log M_\odot)^{-1}$ pc^{-3}.

$$\psi(\log(M)) = \begin{cases} A * e^{[-(log(M)-log(m_c))^2/2\sigma^2]} & M \leq 1M_\odot \\ B * M^{-1.3} & M > 1 \end{cases} \tag{2.12}$$

where A = 0.158 $(\log M_\odot)^{-1}$ pc^{-3}, $m_c = 0.079$, $\sigma = 0.69$ and B = 4.43×10^{-2} $(\log M_\odot)^{-1}$ pc^{-3}. For a Chabrier (2003) IMF, and using the mass limits above, $\alpha_{\text{CCSNe}} = 0.011 M_\odot^{-1}$.

The derivation of constants in 2.9 is as follows. The B02 derives the total synchrotron emission in our galaxy using the result of Berkhuijsen (1984). Berkhuijsen (1984) found the total synchrotron radiation observationally from our Galaxy at 408 MHz: $L_{0.408\text{GHz}} = 6.1 \times 10^{21}$ WHz^{-1}. Assuming a radio slope 0f $\alpha = 0.8$ we convert this to the total synchrotron luminosity at 1.49 GHz: $L_{1.49\text{GHz}} = 2.13 \times 10^{21}$ WHz^{-1}. It is possible to then find the average synchrotron luminosity per supernova event, E^{sync}:

$$E^{sync} = \frac{L_{1.49GHz}}{\nu_{CCSN,MW}} = 1.24 \times 10^{23} WHz^{-1} \tag{2.13}$$

where $\nu_{\text{CCSN,MW}}$ is the rate of CCSN in the Milky Way Galaxy. $\nu_{\text{CCSN,MW}}$ is assumed to be constant and we take $\nu_{\text{CCSN,MW}} = 0.011$yr^{-1} which is calibrated with the Chabrier IMF used in SHARK. B02 and O17 assumes a $\nu_{\text{CCSN}} = 0.015$yr^{-1} which appears to be from Cappellaro & Turatto (2001) and uses a Salpeter IMF. It is this difference in $\nu_{\text{CCSN,MW}}$ that results in the different constants used in this paper than those used in B02 and O17.

An electron's lifetime and the luminosity of a galaxy are both dependent on the magnetic and radiation density fields. Different environments can have differences in these density fields. It is an open question that the FIR/radio correlation is seemingly unaffected by these differences. In order to reconcile this, the Bressan model assumes that the lifetime of synchrotron electrons is much smaller than the fading time of CCSN rate. The Bressan model also assumes that the cosmic ray electrons are injected during the adiabatic phase of SN explosions. On these timescales, the bolometric synchrotron luminosity is

$$L_{bol}^{sync} = \int_0^{min(T,\tau_s^{el})} \nu_{CCSN}(T-t)l^{sync}(t)dt, \qquad (2.14)$$

where t is lookback time, $l^{sync}(t)$ is the synchrotron luminosity of the injected electrons after time t, T is the age of the galaxy and τ_s^{el} is the lifetime of electrons against synchrotron losses. For SFGs, $\tau_s^{el} << T$ and the SFR is almost constant over the last Gyr, the intergral can become

$$L_{bol}^{sync} = \nu_{CCSN} \int_0^{\tau_s^{el}} \frac{dE}{dt}dt = \nu_{CCSN}E^{EI} \qquad (2.15)$$

where $l^{sync}(t) = \frac{dE}{dt}$. Hence, the bolometric synchrotron luminosity scales linearly with nu_{CCSN} with a constant E^{EI}.

Equation 2.15 can also be extended for starburst galaxies. To avoid losses from inverse Comptom scattering, τ_s^{el} must be shorter than that of SFGs (Condon, 1992). On a short time scale, we assume that nu_{CCSN} is constant.

This relation can also be extended to specific luminosities. This is shown in B02 and will not be reproduced here. The critical assumptions is that ν_{CCSN} is constant over electron lifetimes and energy loss is due to synchrotron radiation. B02 also shows that specific luminosity has a very weak dependence on magnetic field and argues that bolometric magnitude has no dependence on magnetic fields. This is because, in integrating from specific to bolometric magnitudes, the limits of integration for frequency match with the limits in energy where the power law electron distribution applies.

The Bressan model also considers the contribution of Supernova Remnants (SNR), noting that other sources provide a negligible contribution. Again we will not reproduce this derivation in detail, but will summarise the key assumptions. Using the surface brightness-diameter (Σ - D) relation from observations made by ??, the authors derive the integrated contribution of a population of SNRs which arise from a burst of instantaneous star formation. Assuming that the lifetime of an SNR is associated with its adiabatic phase (Condon (1992)) and integrating over the past SFR, they then derive the average SNR synchrotron luminosity per SN event to be:

$$E^{SNR} \simeq 0.06E^{sync}. \qquad (2.16)$$

Equation 2.16 tells us that the contribution from SNR makes up about 6 percent of the synchrotron emission. The remaining 94 percent comes from electrons injected into the ISM and accelerated by magnetic fields. As previously derived, $E^{sync} = 1.24 \times 10^{23} WHz^{-1}$ and so $E^{EI} = 1.25 \times 10^{23} WHz^{-1}$, $E^{SNR} = 0.0795 \times 10^{23} WHz^{-1}$.

SNRs have a spectrum which is modelled by $L_\nu = \nu^{\alpha_{SNR}}$ where $\alpha_{SNR} = 0.2 - 0.5$. The Bressan model assumes that the radio slope of SNRs is constant at $\alpha_{SNR} = 0.5$, which is less than the characteristic observed slope of the total non thermal emission of normal galaxies ($\alpha_{sync} = 0.8$). In order to compensate for this, the Bressan model assumes that the spectrum for electrons

injected into the ISM has a radio slope of $\alpha_{\mathrm{EI}} \simeq 0.9$ for an overall synchrotron radio slope of $\alpha_{\mathrm{sync}} = 0.8$.

We differ in our approach to radio slopes. Like the Bressan model we too assume that $\alpha_{\mathrm{SNR}} = 0.5$ but use a $\alpha_{\mathrm{EI}} = 0.816$ since this more accurately produces an overall slope of $\alpha_{\mathrm{sync}} = 0.8$. Solving Equation **??** gives the result of $\alpha_{\mathrm{EI}} = 0.816$.

Implementing the effects of synchrotron self-absorption was considered, however these effects have been shown to be negligible at the brightness temperatures of SFGs (Condon (1992)). Because of this, we do not include the effects of synchrotron self-absorption in this model.

Chapter 3

Results

3.0.1   Local Universe (z = 0)

Comparisons with the GAMA Survey

Radio Luminosity Functions at z = 0

Figure 3.2 shows the radio luminosity function at z = 0 at a frequency of 1.4GHz and 150MHz. The radio luminosity function shows the distribution of galaxies across different bins of luminosity. To find the radio luminosity function I first took a histogram of the log_{10} radio luminosities of all galaxies at z = 0. This histogram is taken over a set of bins with equal bin width. This histogram is then divided by the total volume of the simulation (for all 64 snapshots this is $210\text{Mpc}^3 \times 64$ snapshots) and the bin width of the histogram. The $1 - \sigma$ confidence intervals is then estimated using bootstrapping.

In observations, there can be many sources of error that can affect the results of the radio luminosity function. These can include radio K correction, error in completeness, contamination by AGNs (Novak et al. (2017)), cosmic variance (Driver et al. (2022)) and low sample sizes (Bonato et al. (2021b)). In SHARK, no K correction is required (Though we do assume a constant spectral index of $\alpha = -0.8$) and the resolution is clearly complete. No AGNs are modelled in the radio luminosities so contamination cannot occur. Any affect from cosmic variance would be very low since the volume of the sample is $13,440Mpc$. Finally, our sample sizes are very large due to the computational ease by which galaxies are modelled.

In order to estimate the effects that the results of these errors can have on the radio luminosity function I convolve the radio luminosity function. During convolution, each individual galaxy luminosity is mulitplied by a random constant, before binning. This constant is chosen from a random Gaussian with a mean of 0 and a standard deviation of 0.3. Convolving luminosities in this way provides an analogue estimation of errors made in observations. This process is the same for both frequencies. The convolved radio luminosity function is shown in red and the non-convolved radio luminosity function is shown in blue.

The result of this is compared with the observational results from Bonato et al. (2021a), Butler et al. (2019), Novak et al. (2017) and Ocran et al. (2019) (for 1.4GHz) and with Bonato et al.
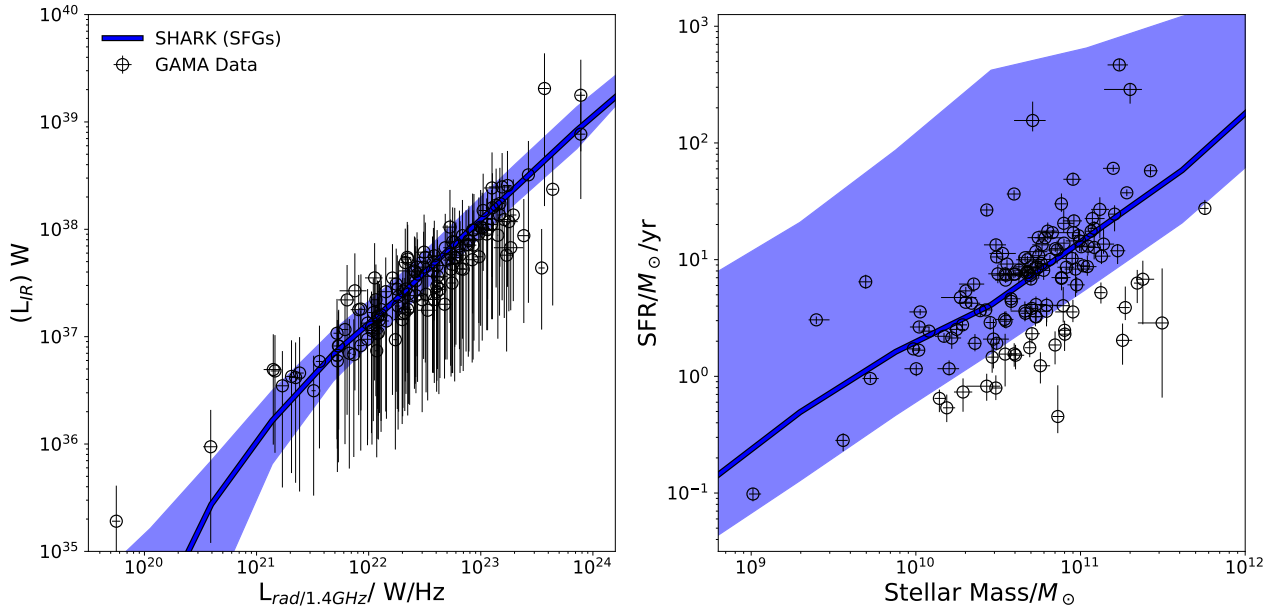
Figure 3.1: Comparison plots with observational data of individual SFGs from the GAMA survey. In both plots, the circles are observational data from the GAMA survey and the blue area is representations from SHARK using our radio model. The left plot shows the L_IR vs. L_rad(1.4GHz) for these two populations. In this plot, the area in blue around the median line represents 1-σ uncertainty. The right plot shows SFR vs. total stellar mass where the shaded blue region shows the full extent of the galaxy population, hence the extent of our definition of SFGs. Both plots contain the same galaxies from the GAMA survey and the same subset of galaxies from SHARK. In this subset we have chosen all SFGs at z = 0, withing the stellar mass range of $8 \leq \log(M/M_\odot) \leq 12$ and with a total infrared luminosity greater than 10^{35}W.
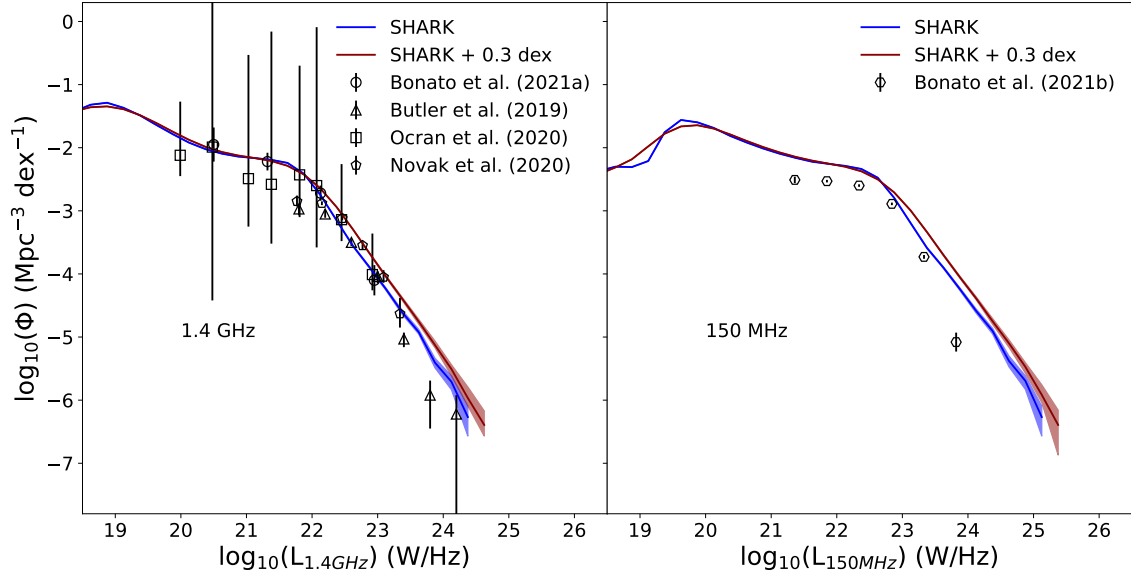
Figure 3.2: The radio luminosity function for all galaxies at z = 0 for frequencies 1.4GHz (left) and 150MHz (right). *Left*: The blue line shows the luminosity function with no convolution while the dark red line shows the luminosity function convolved with a Gaussian with a mean of 0 and a standard deviation of 0.3. Errors have been approximated using bootstrapping and the $1 - \sigma$ lines are shown in the shaded regions about the median line. Comparisons are made with observational data of SFGs from Bonato et al. (2021a), Butler et al. (2019) (This data also includes high-excitation sources for which star formation is the likely cause of their radio emission), Novak et al. (2017) and Ocran et al. (2019). *Right*: Same as the left plot except at 150MHz. Comparisons are made with observational data of SFGs from Bonato et al. (2021b).

3. RESULTS

(2021b) (for 150MHz). These all show for SFGs, though different methods have been used to determine the presence of AGNs and to quantify the errorbars.

Bonato et al. (2021a) (from which these observational results are sourced) used data from the Westerbork Synthesis Radio Telescope (WSRT) to derive the radio luminosity function. This survey covered an area of ~ 1.4 deg^2 and to a redshift of z ~ 3.2. Radio Loud AGNs are removed using a radio threshold and a radio/SFR threshold. Radio Quiet AGNs are classified using the criterion from Messias et al. (2012). Error bars only show the Poisson error of the sample.

Butler et al. (2019) used the Australia Telescope Compact Array (ATCA) to obserse an area of ~ 25 deg^2 to a redshift of z ~ 1.3. AGNs are removed using a decision tree in Butler et al. (2018). This decision tree uses: (i) X-Ray Luminosities and Hardness ratios, (ii) SED fitting, (iii) Mid-Infrared colours, (iv) Optical Spectra, (v) Optical colours and (vi) Radio Luminosities, spectral indices and morphologies to decide whether a source contains an AGN or not. Despite this comprehensive method of AGN cleaning, Butler et al. (2018) ackowledges that AGN contamination is still possible within their data. The error bars here represent the standard deviation of the inverse completeness fraction.

Novak et al. (2017) used the Very Large Array (VLA) covering an area of 2 deg^2 to a redshift of z ~ 5. The authors did not remove all AGNs from their sample, rather only radio loud AGNs. The radio loud aGNs were removed with SED fitting. The error bars here are the Poisson error of the sample and does not include errors from radio K correction, sample completeness or radio quiet AGN contamination.

Ocran et al. (2019) used the Giant Meterwave Radio Telescope (GMRT) to measure an area of 1.2 deg^2, to a redshift z ~ 5 at 610MHz. They use the sample from Ocran et al. (2020) and convert to 1.4GHz by assuming a constant spectral index of $\alpha = -0.8$. AGNs are removed using the following diagnostics: (i) a radio cutoff, (ii) the mid-infrared radio ratio, (iii) X-Ray luminosity, (iv) colour-colour diagram and (v) the use of BOSS CLASS and SUB CLASS (Bolton et al. (2012)). Error bars are calculated using confidence tables from Gehrels (1986).

For the 150MHz radio luminosity function, Bonato et al. (2021b) used data from the Low Freqeuncy Array (LOFAR). They use SED fitting to determine AGNs. Error bars are the the quadratic sums of the Poisson uncertainty and sample variance.

At z = 0, we find excellent agreement in the radio luminosity function at 1.4GHz. At this frequency, the non-convolved line appears to agree more with the observational data than the convolved line. This shows the accuracy with which SHARK and the radio model employed here has at least at z = 0.

For 150MHz however, we do not get good agreement with the data with either the convolved or the non-convolved data. One possible explanation for this is that Bonato et al. (2021b) does not adequately estimate the error of the radio luminosity function. The data from Bonato et al. (2021b) would include errors due to cosmic variance and low sample sizes. Bonato et al. (2021b) measured the galaxies at 150MHz, so there's no K correction. If AGN contamination was an issue, then this would increase the radio luminosity of the points from Bonato et al. (2021b); the points would appear above the SHARK lines instead of below. Including error from cosmic
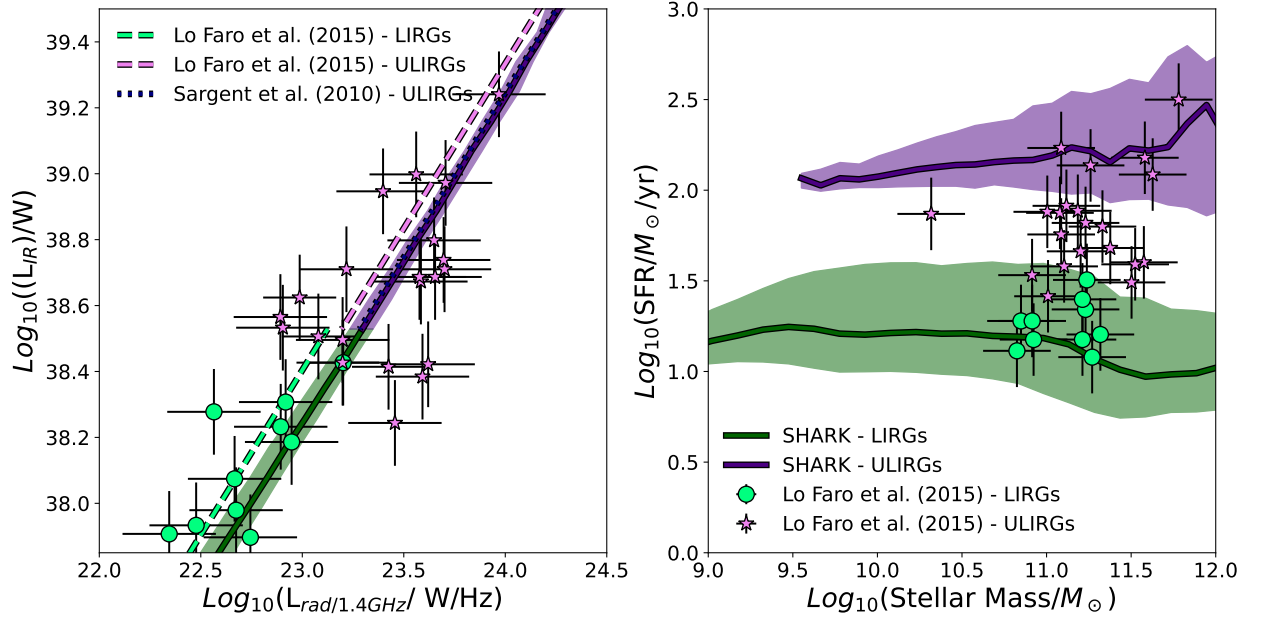
Figure 3.3: Comparison plots with observational data of individual (U)LIRGs from Lo Faro et al. (2015). As in 3.1, the circles are the observational data from Lo Faro et al. (2015) of LIRGs and stars are ULIGRs. The blue area is LIRGs and the red area is ULIRGs from the SHARK with radio luminosity calculated using our model. The right plot shows L_IR vs. L_rad(1.4GHz) and the left plot shows SFR vs. total stellar mass. LIRGs from SHARK have been selected as having a total $10^{11}L_\odot < L_{IR} < 10^{12}L_\odot$ and ULIRGs have been selected as having a total $10^{12}L_\odot > L_{IR}$. These are the same parameters that constrain the (U)LIRGs found in Lo Faro et al. (2015). No selection with redshift have been made of the SHARK galaxies.

variance and low sample sizes would mean error bars much larger than the Poisson error shown in the points in Fig. 3.2. If such error was added to these points, it's likely that SHARK and these measurements would agree.

This disagreement with the data could also be caused by a low SFR function in SHARK(CITE CITE CITE). Please see section XYZ where this is discussed.

Overall the radio luminosity functions at z = 0 agree with observations. The estimation of errors from observations is problematic for both $1.4GHz$ and $150MHz$ frequencies, but more so at $150MHz$.
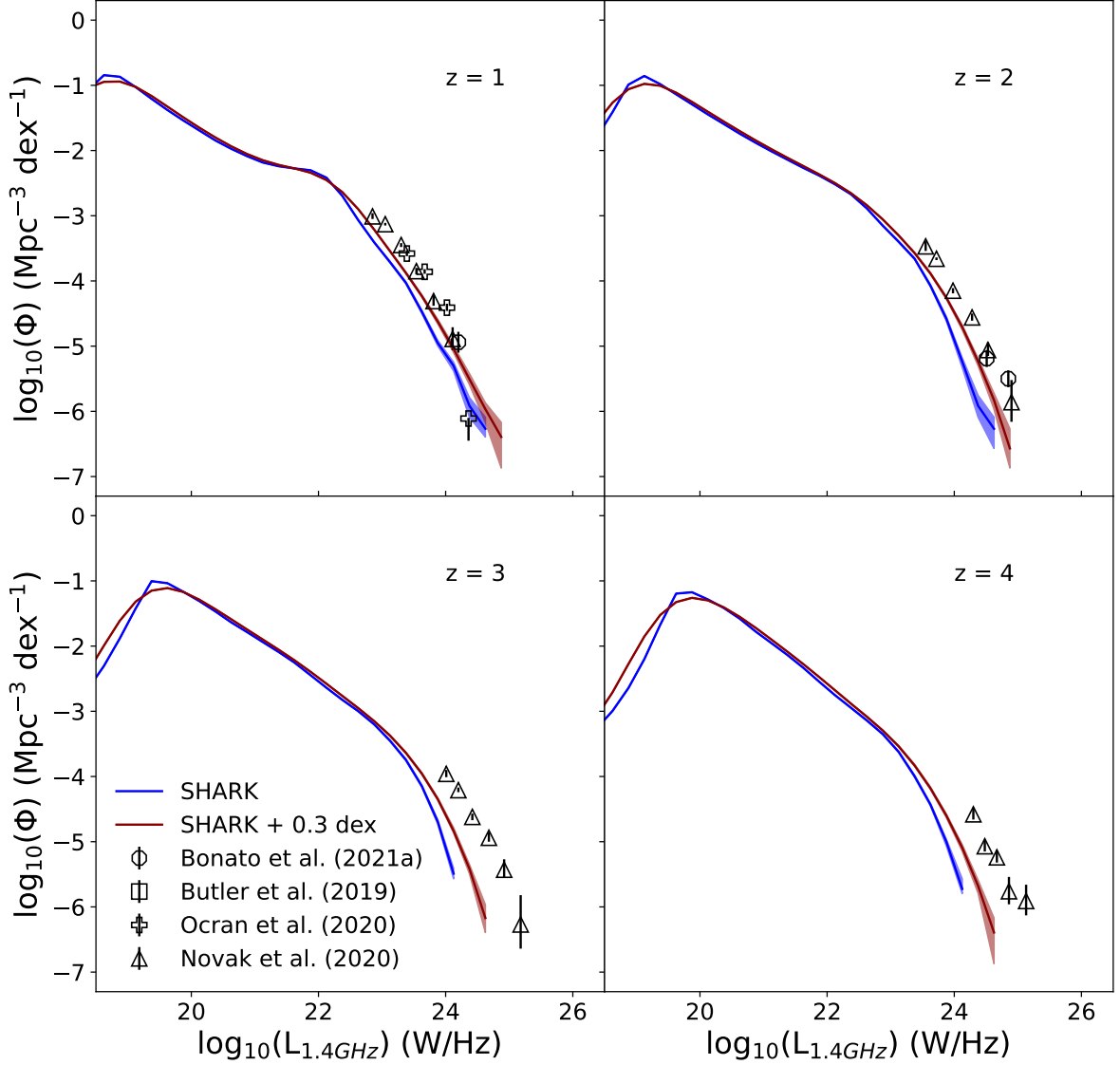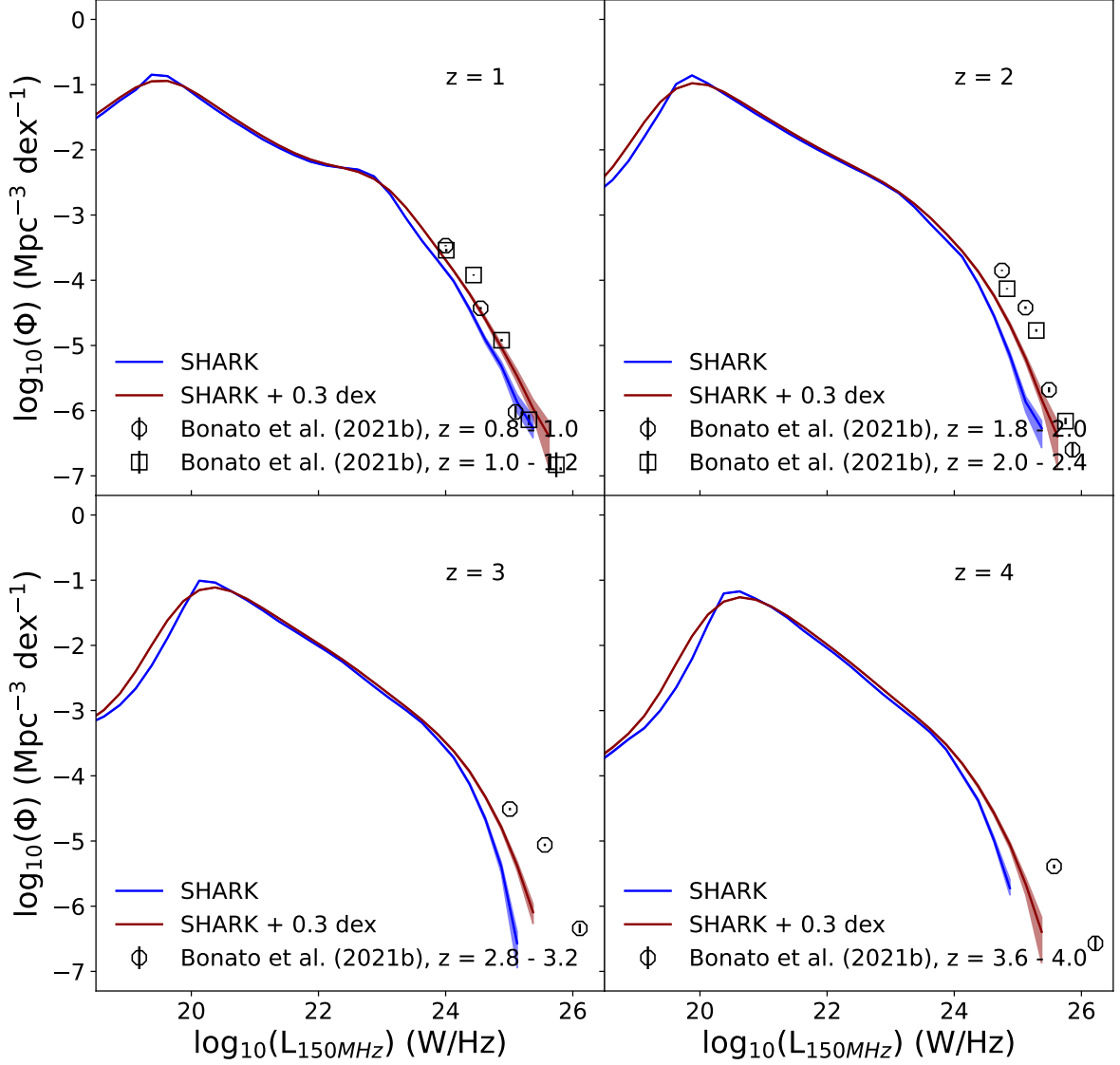
Figure 3.4: The radio luminosity function for all galaxies for different redshifts for frequency of 1.4GHz. Top-left panel shows z = 1, top right panel shows z = 2, bottom left panel shows z = 3 and bottom right panel shows z = 4. Much of the details here are the same as in Fig. 3.2; the blue line shows the median with no convolution and the orange shows the same but convolved with a Gaussian with mean = 0 and 0.3 standard deviation. Comparisons are made with observational data of SFGs from Bonato et al. (2021a), Butler et al. (2019), Novak et al. (2017) and Ocran et al. (2019). The shaded reagion shows the $1 - \sigma$ area estimated using bootstrapping.

Figure 3.5: The radio luminosity function for all galaxies for different redshifts for frequency of 150MHz. As in Fig. 3.4, top-left panel shows z = 1, top right panel shows z = 2, bottom left panel shows z = 3 and bottom right panel shows z = 4. Much of the details here are the same as in the right hand panel of Fig. 3.2; the blue line shows the median with no convolution and the orange shows the same but convolved with a Gaussian with mean = 0 and 0.3 standard deviation. Comparisons are made with observational data of SFGs from Bonato et al. (2021b) The shaded reagion shows the $1 - \sigma$ area estimated using bootstrapping.
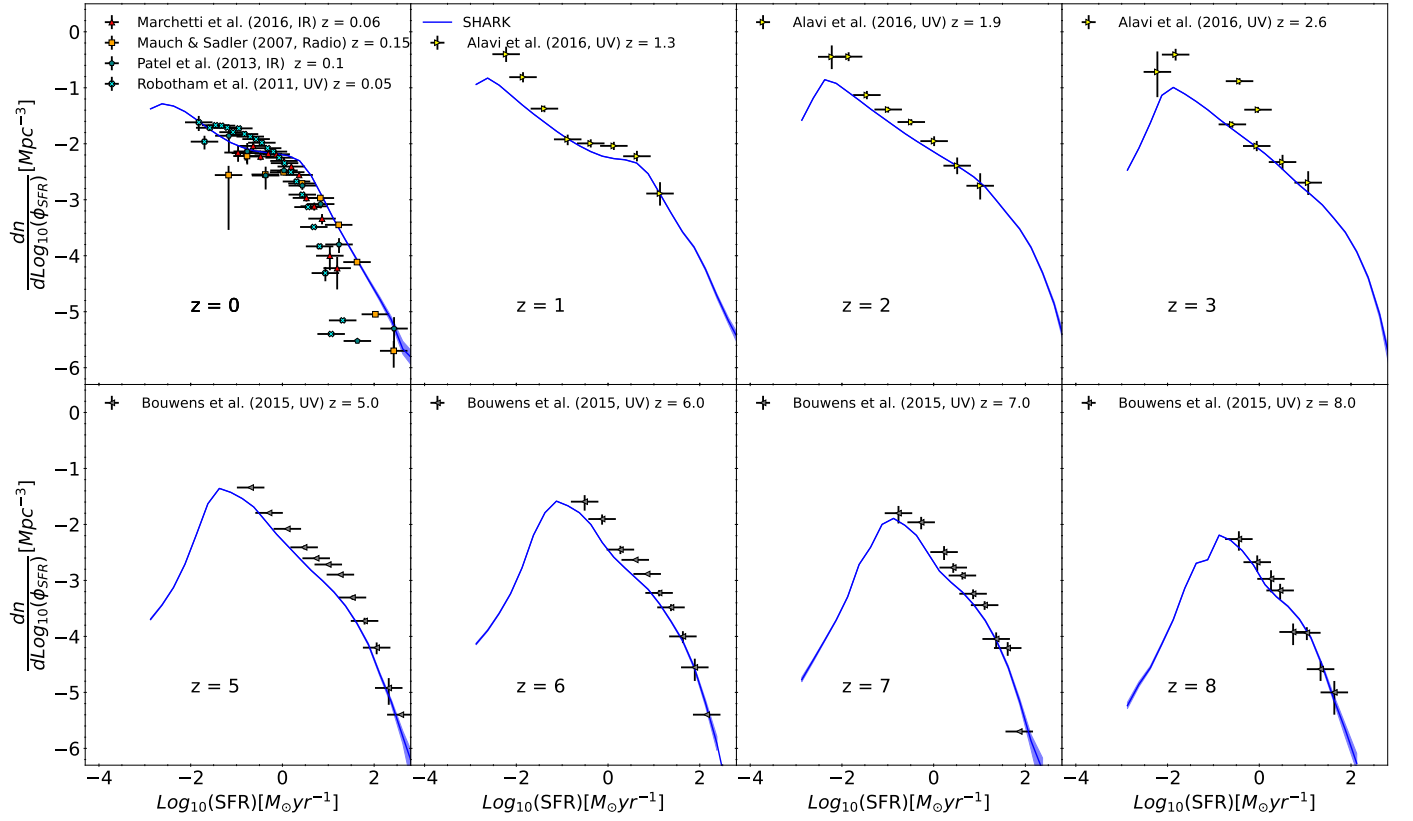
Figure 3.6: . The SFR function compared with data from many sources.
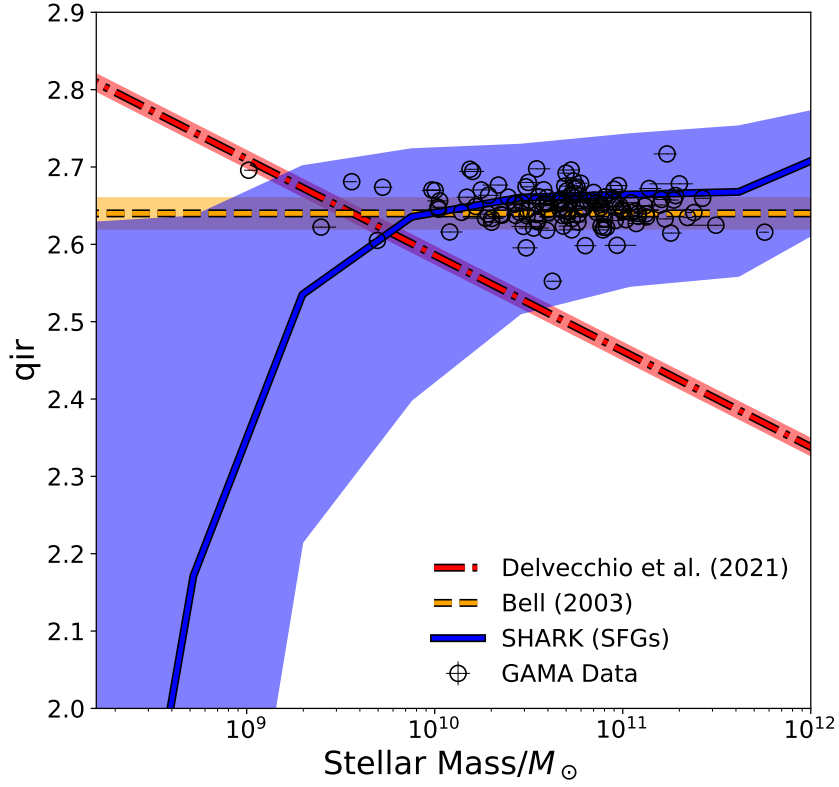
Figure 3.7: qir vs. total stellar mass compared with observational data of individual galaxies from the GAMA survey. These are the same galaxies as in Fig. 3.1. The blue region shows galaxies from SHARK, with the thick line being the median result and the shaded blue region showing $1 - \sigma$ uncertainty. The red dot-dashed line shows the qir vs. total stellar mass relationship found in Delvecchio et al. (2021) (Fig. 14 in that paper). The orange dashed line shows the constant qir found in Bell (2003).
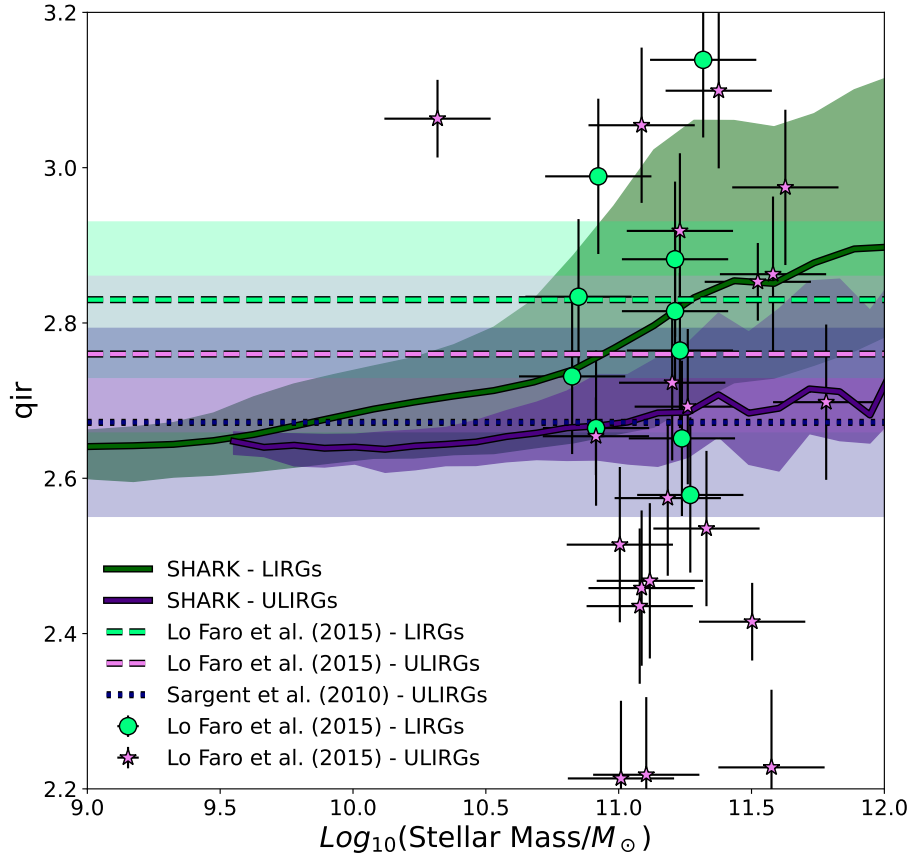
Figure 3.8: Comparison plots with observational data of individual (U)LIRGs from Lo Faro et al. (2015) of qir vs. total stellar mass. As in Fig. 3.3, the stars and circles are observational data of (U)LIRGs from Lo Faro et al. (2015). The red and blue areas are (U)LIRGs selected from SHARK with the same selection as in Fig. 3.3.

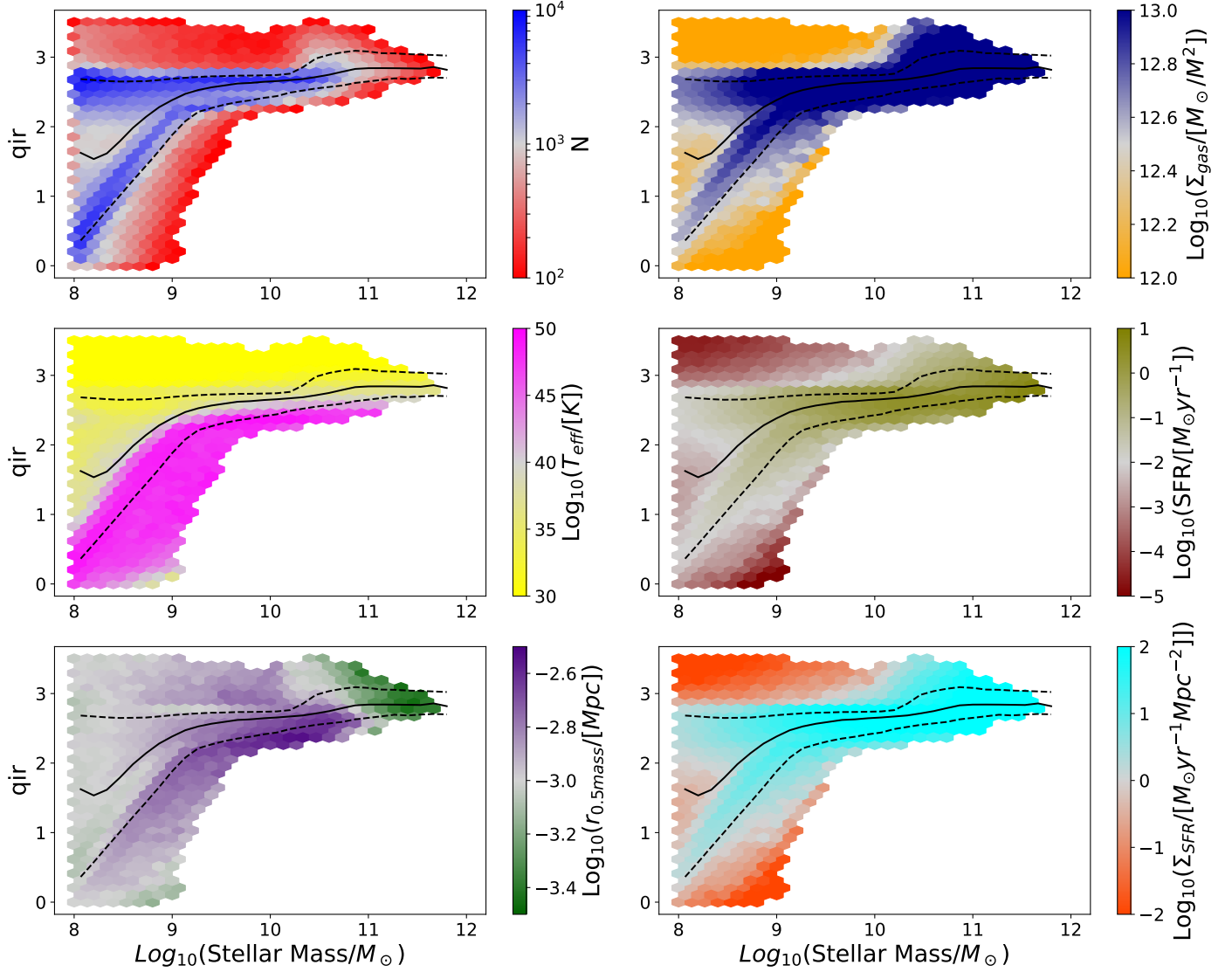**Figure 3.9:** qir vs. total stellar mass coloured by different parameters. Upper left most panel shows number counts. Upper right panel shows coloured by effective dust temperature. Lower left panel shows coloured by half mass radius and lower right panel shows coloured by gas surface density. Solid black line shows the median qir evolution with total stellar mass and the dashed black lines show $1 - \sigma$ uncertainty.
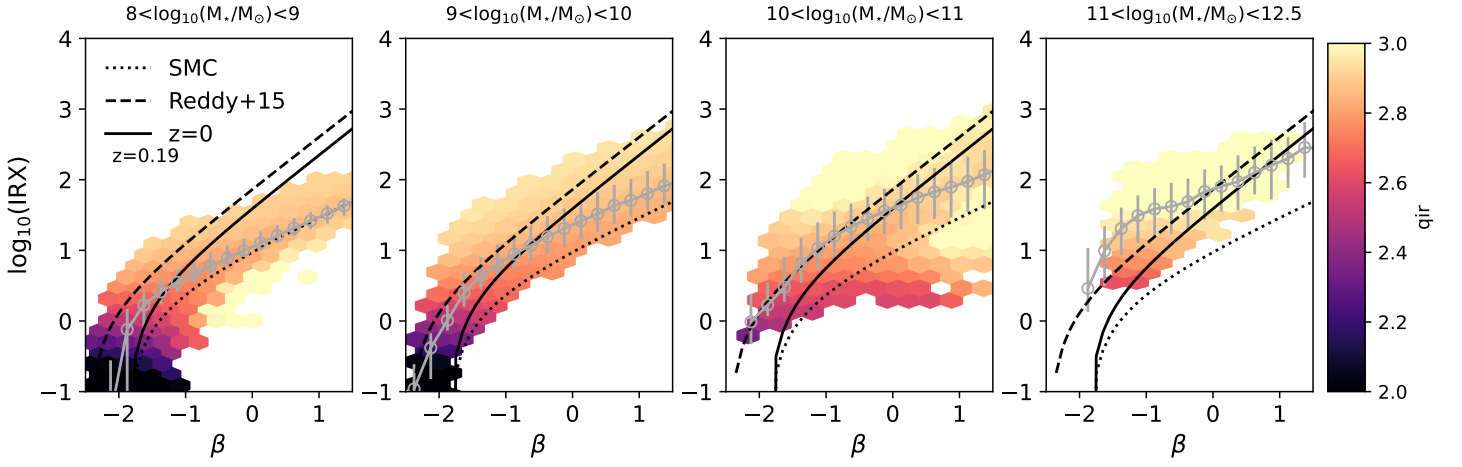
3. RESULTS

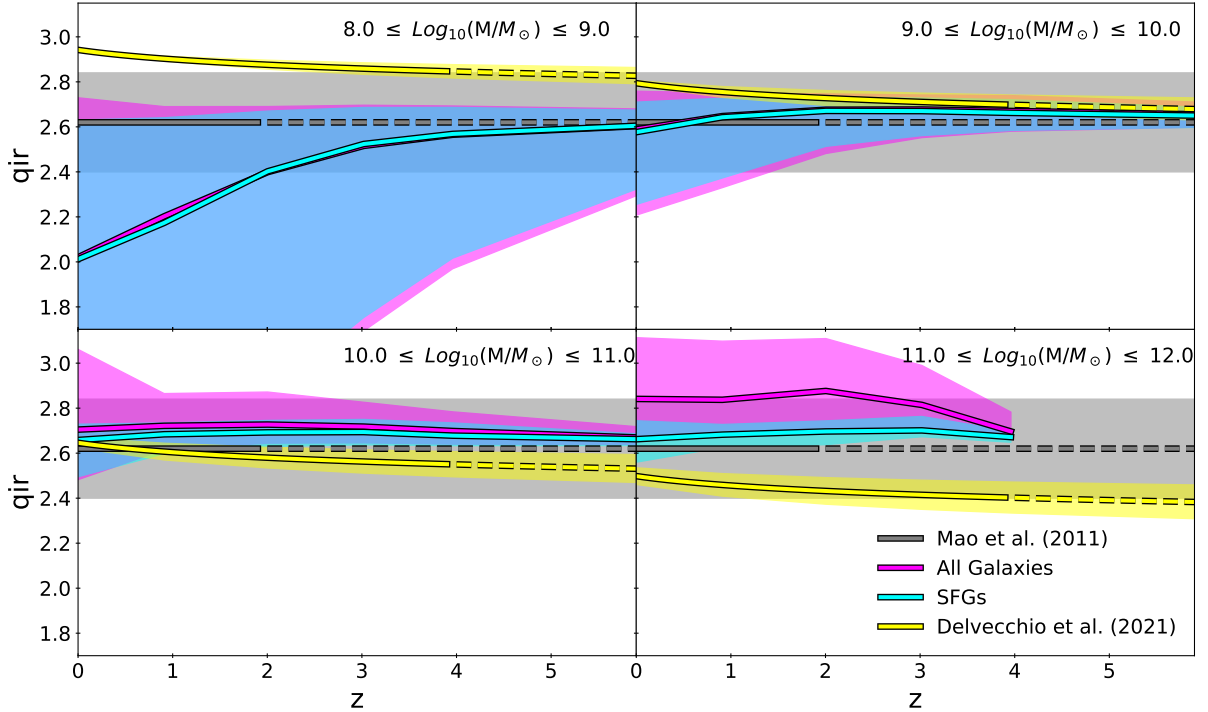**Figure 3.10:** IRX-Beta function plot at z = 0.19 coloured by qir.

Figure 3.11: qir vs. z for different stellar mass bins. Solid line shows the median and the shaded regions show the $1 - \sigma$ uncertainty.

3.0.2   z > 0

3.0.3   The Far-Infrared Radio Correlation

Comparisons with the literature

qir and extinction

qir vs. z

3.0.4   Number Counts

Lightcone

Number counts with z
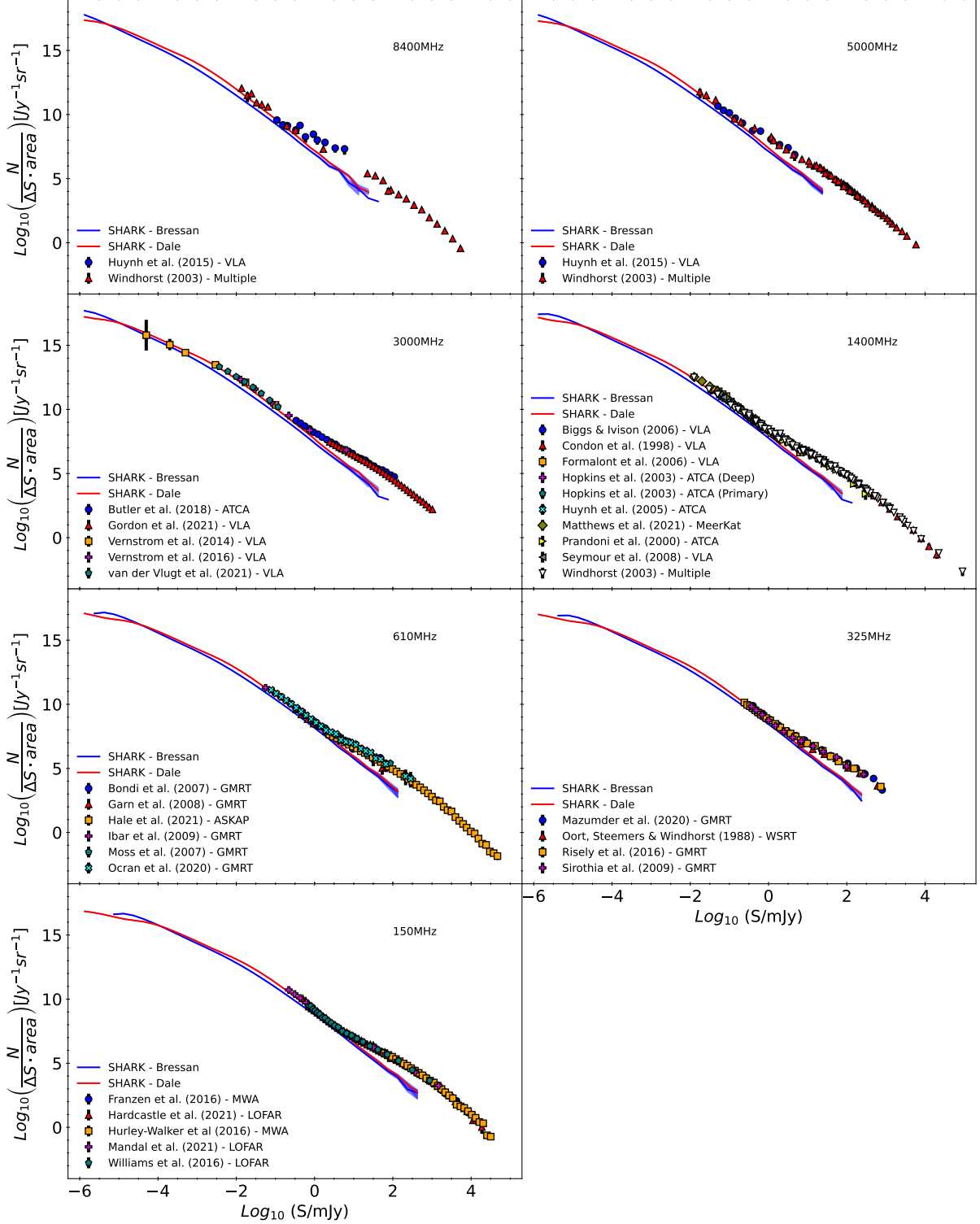
Stellar Mass and SFR with z

Figure 3.12: The number counts per redshift for different radio frequencies for all galaxies with $/rmS > 10^{-2} mJy$. Solid lines are the median line and the shaded area represents $1 - \sigma$ estimated using bootstrapping.
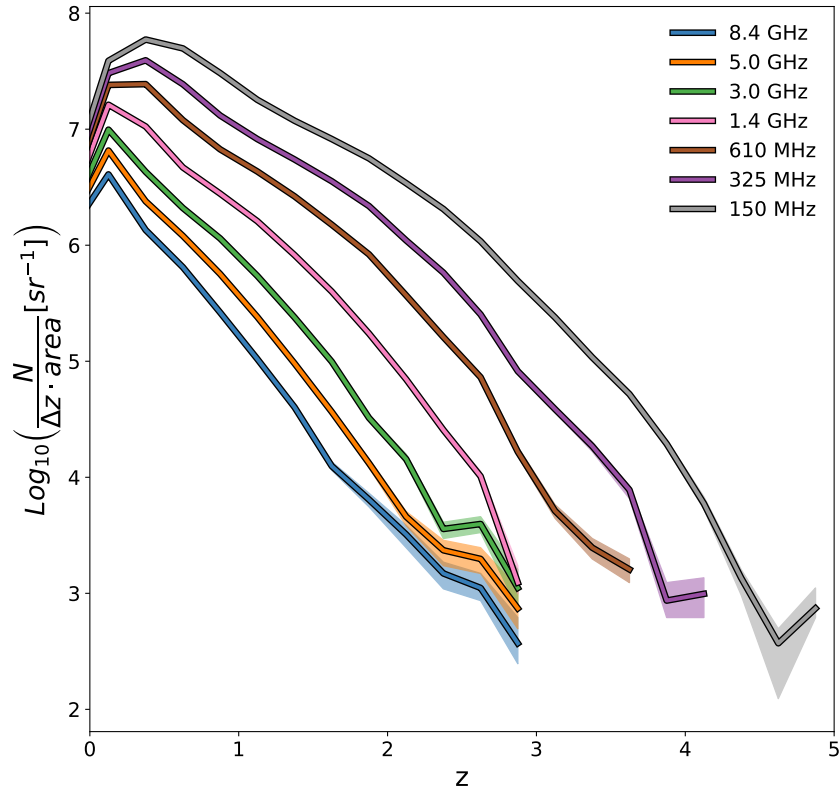
Figure 3.13: The number counts per redshift for different radio frequencies for all galaxies with S > 10^{-2}mJy. Solid lines are the median line and the shaded area represents $1 - \sigma$ estimated using bootstrapping.
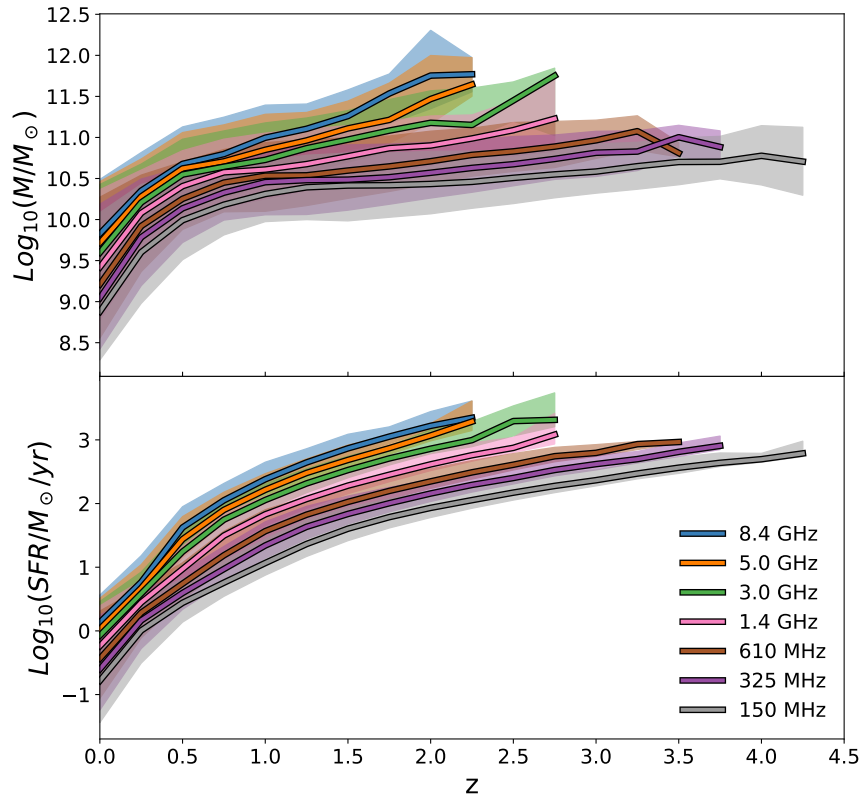
Figure 3.14: Upper panel shows the median total stellar mass of all galaxies with S > 10^{-2}mJy for different radio frequencies. Shaded area represents $1 - \sigma$ region. Lower panel shows the same but median SFR.

Chapter 4

Discussion

4.1   TBD

TEXT

Chapter 5

Conclusion

TBD

Chapter 6

Future Work

TBD

References

Algera H., et al., 2020, The Astrophysical Journal, 903, 138

Anderson L., Bania T., Jackson J., Clemens D., Heyer M., Simon R., Shah R., Rathborne J., 2009, The Astrophysical Journal Supplement Series, 181, 255

Ando S., Sato K., Totani T., 2003, Astroparticle Physics, 18, 307

Appleton P., et al., 2004, The Astrophysical Journal Supplement Series, 154, 147

Bell E. F., 2003, The Astrophysical Journal, 586, 794

Berkhuijsen E., 1984, Astronomy and Astrophysics, 140, 431

Bolton A. S., et al., 2012, The Astronomical Journal, 144, 144

Bonato M., Prandoni I., De Zotti G., Brienza M., Morganti R., Vaccari M., 2021a, Monthly Notices of the Royal Astronomical Society, 500, 22

Bonato M., et al., 2021b, Astronomy & Astrophysics, 656, A48

Bourne N., Dunne L., Ivison R., Maddox S., Dickinson M., Frayer D., 2011, Monthly Notices of the Royal Astronomical Society, 410, 1155

Bressan A., Silva L., Granato G. L., 2002, Astronomy & Astrophysics, 392, 377

Bruzual G., Charlot S., 2003, Monthly Notices of the Royal Astronomical Society, 344, 1000

Butler A., et al., 2018, Astronomy & Astrophysics, 620, A16

Butler A., Huynh M., Kapińska A., Delvecchio I., Smolčić V., Chiappetti L., Koulouridis E., Pierre M., 2019, Astronomy & Astrophysics, 625, A111

Cañas R., Elahi P. J., Welker C., Lagos C. d. P., Power C., Dubois Y., Pichon C., 2019, Monthly Notices of the Royal Astronomical Society, 482, 2039

Cappellaro E., Turatto M., 2001, in , The influence of binaries on stellar population studies. Springer, pp 199–214

Chabrier G., 2003, Publications of the Astronomical Society of the Pacific, 115, 763

Charlot S., Fall S. M., 2000, The Astrophysical Journal, 539, 718

Chauhan G., Lagos C. d. P., Obreschkow D., Power C., Oman K., Elahi P. J., 2019, Monthly Notices of the Royal Astronomical Society, 488, 5898

Condon J., 1992, Annual review of astronomy and astrophysics, 30, 575

Condon J. J., Ransom S. M., 2016, Essential radio astronomy. Vol. 2, Princeton University Press

Dale D. A., Helou G., Contursi A., Silbermann N. A., Kolhatkar S., 2001, The Astrophysical Journal, 549, 215

Dale D. A., Helou G., Magdis G. E., Armus L., Díaz-Santos T., Shi Y., 2014, The Astrophysical Journal, 784, 83

De Jong T., Klein U., Wielebinski R., Wunderlich° E., 1985, Astron. Astrophys, 147, L6

Delhaize J., et al., 2017, Astronomy & Astrophysics, 602, A4

Delvecchio I., et al., 2021, Astronomy & Astrophysics, 647, A123

Donley J., Rieke G., Rigby J., Pérez-González P., 2005, The Astrophysical Journal, 634, 169

Draine B., Anderson N., 1985, The Astrophysical Journal, 292, 494

Driver S. P., et al., 2022, , 513, 439

Duncan K. J., Shivaei I., Shapley A. E., Reddy N. A., Mobasher B., Coil A. L., Kriek M., Siana B., 2020, Monthly Notices of the Royal Astronomical Society, 498, 3648

Désert F.-X., Boulanger F., Puget J.-L., 1990, Astronomy and Astrophysics, 237, 215

Elahi P. J., Welker C., Power C., Lagos C. d. P., Robotham A. S., Cañas R., Poulton R., 2018, Monthly Notices of the Royal Astronomical Society, 475, 5338

Elahi P. J., Cañas R., Poulton R. J., Tobar R. J., Willis J. S., Lagos C. d. P., Power C., Robotham A. S., 2019a, Publications of the Astronomical Society of Australia, 36, e021

Elahi P. J., Poulton R. J., Tobar R. J., Cañas R., Lagos C. d. P., Power C., Robotham A. S., 2019b, Publications of the Astronomical Society of Australia, 36, e028

Gehrels N., 1986, The Astrophysical Journal, 303, 336

Giulietti M., et al., 2022, Monthly Notices of the Royal Astronomical Society, 511, 1408

Heger A., Fryer C. L., Woosley S. E., Langer N., Hartmann D. H., 2003, The Astrophysical Journal, 591, 288

Helou G., Soifer B., Rowan-Robinson M., 1985, The Astrophysical Journal, 298, L7

REFERENCES

Ivison R. J., et al., 2010a, Monthly Notices of the Royal Astronomical Society, 402, 245

Ivison R., et al., 2010b, Astronomy & Astrophysics, 518, L31

Jarvis M. J., et al., 2010, Monthly Notices of the Royal Astronomical Society, 409, 92

Kreckel K., et al., 2013, The Astrophysical Journal, 771, 62

Kregel M., Van Der Kruit P. C., Grijs R. d., 2002, Monthly Notices of the Royal Astronomical Society, 334, 646

Krumholz M. R., 2014, Physics Reports, 539, 49

Krumholz M. R., McKee C. F., Tumlinson J., 2009, The Astrophysical Journal, 699, 850

Lacey C. G., et al., 2016, Monthly Notices of the Royal Astronomical Society, 462, 3854

Lacki B. C., Thompson T. A., Quataert E., 2010, The Astrophysical Journal, 717, 1

Lagos C. d. P., Tobar R. J., Robotham A. S., Obreschkow D., Mitchell P. D., Power C., Elahi P. J., 2018, Monthly Notices of the Royal Astronomical Society, 481, 3573

Lagos C. d. P., et al., 2019, Monthly Notices of the Royal Astronomical Society, 489, 4196

Lo Faro B., Silva L., Franceschini A., Miller N., Efstathiou A., 2015, Monthly Notices of the Royal Astronomical Society, 447, 3442

Magnelli B., et al., 2015, Astronomy & Astrophysics, 573, A45

Mao M. Y., Huynh M. T., Norris R. P., Dickinson M., Frayer D., Helou G., Monkiewicz J. A., 2011, Proceedings of the International Astronomical Union, 7, 404

Messias H., Afonso J., Salvato M., Mobasher B., Hopkins A. M., 2012, The Astrophysical Journal, 754, 120

Mezger P., Henderson A., 1967, The Astrophysical Journal, 147, 471

Molnár D. C., et al., 2021, Monthly Notices of the Royal Astronomical Society, 504, 118

Nomoto K., 1984, The Astrophysical Journal, 277, 791

Norris R. P., et al., 2006, The Astronomical Journal, 132, 2409

Novak M., et al., 2017, Astronomy & Astrophysics, 602, A5

Obi I., et al., 2017, arXiv preprint arXiv:1702.02230

Ocran E., Taylor A., Vaccari M., Ishwara-Chandra C., Prandoni I., Prescott M., Mancuso C., 2019, arXiv preprint arXiv:1912.00934

Ocran E., Taylor A., Vaccari M., Ishwara-Chandra C., Prandoni I., 2020, Monthly Notices of the Royal Astronomical Society, 491, 1127

Omar A., Paswan A., 2018, Monthly Notices of the Royal Astronomical Society, 477, 3552

Oster L., 1961, Reviews of Modern Physics, 33, 525

Pavlović M., 2021, Serbian Astronomical Journal, pp 15–27

Planck Collaboration Ade P. A., et al., 2016, Astronomy & Astrophysics, 594, A13

Read S. C., et al., 2018, Monthly Notices of the Royal Astronomical Society, 480, 5625

Robotham A., Bellstedt S., Lagos C. d. P., Thorne J., Davies L., Driver S., Bravo M., 2020, Monthly Notices of the Royal Astronomical Society, 495, 905

Rubin R. H., 1968, The Astrophysical Journal, 154, 391

Sargent M. T., et al., 2010, The Astrophysical Journal Letters, 714, L190

Schober J., Sargent M., Klessen R., Schleicher D., 2022, arXiv preprint arXiv:2210.07919

Shao L., Koribalski B. S., Wang J., Ho L. C., Staveley-Smith L., 2018, Monthly Notices of the Royal Astronomical Society, 479, 3509

Smith D., et al., 2014, Monthly Notices of the Royal Astronomical Society, 445, 2232

Solarz A., Pollo A., Bilicki M., Pepiak A., Takeuchi T. T., Piatek P., 2019, Publications of the Astronomical Society of Japan, 71, 28

Strömgren B., 2013, in , A Source Book in Astronomy and Astrophysics, 1900–1975. Harvard University Press, pp 588–592

Thomson A., et al., 2014, Monthly Notices of the Royal Astronomical Society, 442, 577

Tran Q., et al., 2001, The Astrophysical Journal, 552, 527

Trayford J. W., et al., 2017, Monthly Notices of the Royal Astronomical Society, 470, 771

Trayford J. W., Lagos C. d. P., Robotham A. S., Obreschkow D., 2019, arXiv preprint arXiv:1908.08956

Tsujimoto T., Yoshii Y., Nomoto K., Matteucci F., Thielemann F.-K., Hashimoto M., 1997, The Astrophysical Journal, 483, 228

Van Der Kruit P., 1973, Astronomy and Astrophysics, 29, 263

Van den Heuvel E., Yoon S.-C., 2007, Astrophysics and Space Science, 311, 177

REFERENCES

Van der Kruit P., 1971, Astronomy and Astrophysics, Vol. 15, p. 110-122, 15, 110

Vazdekis A., Koleva M., Ricciardelli E., Röck B., Falcón-Barroso J., 2016, Monthly Notices of the Royal Astronomical Society, 463, 3409

Völk H., 1989, Astronomy and Astrophysics, 218, 67

Vollmer B., Soida M., Dallant J., 2022, Astronomy & Astrophysics, 667, A30

Yun M., Carilli C., 1999, Science with the Atacama Large Millimeter Array (ALMA), p. 78

Yun M. S., Reddy N. A., Condon J., 2001, The Astrophysical Journal, 554, 803

TEXT

TEXT